2. L. Spitzer, *Physics of Fully Ionized Gases*, 2nd Rev. Ed. (Interscience, New York, 1962), p. 148.

3. W. J. Karzas and R. Latter, *Astrophys. J. Supp.* **6**, 167 (1961).

4. B. L. Henke and R. L. Elgin, *Advances in X-Ray Analysis* **13**, 1 (1969).

5. R. Epstein, S. Skupsky, and J. Delettrez, *J. Quant. Spectrosc. Radiat. Transfer* **35**, 131 (1986).

6. R. Epstein, *Phys. Fluids B* **1**, 214 (1989).

1.C Fokker-Planck Simulations of Laser Filamentation in Plasmas

In inertial confinement fusion (ICF), where irradiation uniformity is a crucial issue, it is important to understand the process of laser-filamentation instability.[1] The breakup of laser light into filaments occurs as a result of plasma density depressions that form localized focusing channels. The density depressions may be caused either by ponderomotive forces[2] due to laser-plasma interactions or by thermal forces[3] arising from collisional light absorption. The main consequences of the instability are that high-intensity laser irradiation in the filaments can generate ablation-pressure nonuniformities in ICF targets and give rise to undesirable parametric instabilities.[1]

There have been extensive theoretical and experimental efforts to understand and characterize filamentation.[1-6] Recently, Young *et al.*[4] have attempted to generate and identify filaments under controlled experimental conditions, in which a fairly homogeneous plasma was irradiated by a spatially modulated laser beam. By comparing their observations with analytic predictions based on ponderomotive and thermal-filamentation growth rates, they concluded that the ponderomotive mechanism was responsible for the occurrence of filaments. However, a subsequent improved theory of filamentation that took into account nonlocal heat transport effects indicated that the thermal rather than the ponderomotive mechanism may have been responsible for their experimental observations.[5] The main purpose of this article is to confirm this hypothesis by simulating as closely as possible the reported experimental conditions using the two-dimensional (2-D) Fokker-Planck (FP) code SPARK.[7] Also, by doing parallel simulations invoking classical transport [with Spitzer-Härm[8] (SH) heat flow], general contributions from kinetic effects are demonstrated.

In contrast to the analytic theories that assume linear departure from energy and momentum balance to calculate exponential growth rates, the code models the full hydrodynamic response of the ions (assumed cold), the electron heat flow using the FP equation, and the paraxial wave equation for the laser light. The following sections describe the modeling in more detail, Young *et al.*'s experimental conditions and results, the simulation results, and finally the discussion and conclusions.

Description of the Model

In this article the plasma is assumed to be in planar x-z geometry, where z is the direction of laser propagation. The present version of the 2-D Eulerian code SPARK is comprised of three main parts: (A) a laser-propagation routine based on the paraxial wave equation; (B) an electron-transport routine that solves the FP equation in the center-of-mass frame of the ions; and (C) an ion-transport routine that advances ion density and momentum under the influence of the electron and ponderomotive pressures. These are described briefly as follows.

(A) Laser Propagation

Using the paraxial approximation, the time-averaged electric field $\mathbf{E}_L(x,z)$ of a laser is defined by[3]

$$\mathbf{E}_L(x,z) = \left[\frac{8\pi}{c^2 k(z)}\right]^{1/2} F(x,z)\exp\left[i\int_0^z k(z')dz'\right],\qquad(1)$$

where $k(z) = (\omega/c)\,[1-\omega_p^{\,2}(0,z)/\omega^2]^{1/2}$, ω_p is the plasma frequency, and ω is the angular frequency of the laser. Substituting Eq. (1) for the electric field into Maxwell's equations, we obtain the following result [3]

$$\frac{\partial \mathbf{F}}{\partial z} = \frac{i}{2k}\left\{\frac{\partial^2 \mathbf{F}}{\partial x^2} - \frac{\omega_p^2(x,z)}{c^2}\left[1 - \omega_p^2(0,z)\,/\,\omega_p^2(x,z)\right]\mathbf{F} + ik(z)K_{ib}(x,z)\mathbf{F}\right\},\quad(2)$$

where K_{ib} is the attenuation coefficient for collisional absorption. This so-called paraxial wave equation assumes that the light wave propagates infinitely fast across the plasma and that $|k(z)^{-1}(\partial \mathbf{F}/\partial z)| \ll |\mathbf{F}|$. Its numerical solution is accomplished via standard finite difference techniques (see Ref. 6).

(B) Electron Transport

The electron-transport model is based on the diffusive approximation to the FP equation, without magnetic fields. Such a model has been successfully used to model 2-D electron transport in laser-produced plasmas.[7] Although the equations and methods of solution have been described in detail in Ref. 7, a few modifications have been introduced here. By defining the electron-distribution function in the frame of the moving ions (with velocity $\mathbf{u}_i$), the equations describing the evolution of the isotropic and anisotropic part of the distribution become

$$\frac{\partial f_0}{\partial t} + \mathbf{u}_i \cdot \nabla f_0 - \nabla \cdot \mathbf{u}_i \frac{v}{3}\frac{\partial f_0}{\partial v}$$

$$= -\frac{v}{3}\nabla \cdot \mathbf{f}_1 + \frac{1}{v^2}\frac{\partial}{\partial v}\left\{\frac{v^2}{3}\mathbf{a} \cdot \mathbf{f}_1 + Y\left[Cf_0 + \left(D + \frac{nZ^* v_0^2}{6v}\right)\frac{\partial f_0}{\partial v}\right]\right\},\quad(3a)$$

$$\mathbf{f}_1 = -\tau\left(v\nabla f_0 - \mathbf{a}\partial f_0\,/\,\partial v\right),\qquad(3b)$$

143

where $\mathbf{a} = |e|\mathbf{E}/m$, $Y = 4\pi(e^2/m)^2 \ln\Lambda$, e is the electric charge, m is the electron mass, $\ln\Lambda$ is the Coulomb logarithm, C and D are the Rosenbluth potentials (defined in Ref. 9), v_0 is the electron oscillatory velocity in the laser field, and $Z^* = \langle Z^2 \rangle / \langle Z \rangle$ is the effective ionization number (where $\langle \rangle$ denotes an average over the ion species). Here the 90° angular scattering collision time is given by $\tau = v^3/[\phi Z^* n Y]$, where $n = \langle Z \rangle n_i$ is the electron number density (assuming quasi-neutrality) and $\phi = (Z^* + 4.2)/(Z^* + 0.24)$. The inclusion of a factor ϕ in the definition of τ is an attempt at correcting for the high-Z (or Lorentz) approximation in Eq. (3b). Such a correction is found to give the *exact* heat flow coefficient when f_0 is Maxwellian.

The second and third terms on the left-hand side of Eq. (3a) represent the hydrodynamic contribution to the transport. For computational purposes it has been found convenient to rewrite them in the form

$$\nabla \cdot (\mathbf{u}_i f_0) - \nabla \cdot \mathbf{u}_i \left(1 + \frac{v}{3} \frac{\partial}{\partial v} \ln f_0 \right) f_0 ,$$

such that the first term is now expressed in conservative form. The reason for using a logarithmic derivative in the second term is that it can be approximated as $\partial_v \ln f_{0,j} = [\ln(f_{0,j+1}/f_{0,j-1})]/2\Delta v_j$, where Δv_j is the magnitude of the velocity mesh at the jth cell. This formulation ensures zero truncation error for a Maxwellian f_0 and minimizes departures from quasi-neutrality.

The solution for f_0 is accomplished by substituting Eq. (3b) into (3a) and differencing the result in an orthogonal mesh (x_l, z_k, v_j), where the subscripts denote cell centers. The left-hand side of Eq. (3a) is advanced explicitly in time using a standard donor-cell scheme.[10] The remaining part of the equation is solved by an "alternating-direction-implicit" method, in the manner described in Ref. 7. Quasi-neutrality is enforced by requiring zero current $\mathbf{j} = -(4\pi e/3)\int dv \, v^3 \mathbf{f}_1$ and calculating the electric field accordingly.

(C) Ion Transport

Conservation of density and momentum for cold ions is given by

$$\frac{\partial n_i}{\partial t} + \nabla \cdot (n_i \mathbf{u}_i) = 0 , \tag{4}$$

$$\frac{\partial (n_i m_i \mathbf{u}_i)}{\partial t} + \nabla \cdot (n_i m_i \mathbf{u}_i \mathbf{u}_i) = -\nabla p + \mathbf{P}_F , \tag{5}$$

where m_i is the ion mass, $p = (4\pi/3)\int dv \, v^4 f_0$ is the electron pressure,

$$\mathbf{P}_F = -\frac{\omega_p^2(x,z)}{2\omega^2} \nabla \left[\frac{|\mathbf{F}|^2}{v_g(z)} \right]$$

is the ponderomotive force, and where $v_g = k(z)c^2/\omega$ is the group velocity of the light wave. Equations (4) and (5) are solved using donor-cell differencing (without artificial viscosity).

At each time step, SPARK solves not only Eqs. (1) to (5) but also an equivalent set of equations where Eq. (3) becomes the energy conservation relation under the assumption of classical heat transport,[8] i.e., $q_{SH} = -\kappa_{SH} \nabla T$, with κ_{SH} being the SH heat-flow coefficient. In order to ensure a meaningful comparison between classical and kinetic transport results, the code is regularly tested in the collisional limit where both are expected to converge.

Young *et al.*'s Experimental Conditions and Results

In Young *et al.*'s[4] experiment a CH-foil target was irradiated by laser light to form a fairly homogeneous underdense plasma. The plasma was subsequently irradiated by a 1.06-μm interaction beam with a 100-ps FWHM pulse. This beam was spatially modulated in the transverse x direction, such that $\delta I/I_0 = 0.81$, where I_0 is the peak laser intensity and $\delta I = (I_0 - I_{min})$. A separate 0.35-$\mu$m beam with the same pulse length was synchronized with the interaction beam to probe for the formation of filaments. The refraction of the probe light through the plasma gave a measure of its density modulation $\delta n/n_0$, which in turn provided an indirect measure of the level of filamentation.

It was reported that, for a transverse spatial modulation $\lambda_\perp = 42$ μm and $I_0 = 4.2 \times 10^{13}$ W/cm^2, laser filamentation was observed with an estimated $\delta n/n_0 \sim 10\%$. No filamentation was observed for a 135-μm wavelength with $I_0 = 4.2 \times 10^{13}$ W/cm^2, nor for a 42-μm wavelength with $I_0 = 2.8 \times 10^{13}$ W/cm^2.

The plasma background conditions at the time of the interaction beam have been simulated by LASNEX, the results of which were presented in Young *et al.*'s paper.[4] For our purpose the plasma is assumed to have a spatial extent of 400 μm, with a parabolic density profile in the z direction approximated by

$$\frac{n}{n_c} = 0.25\left[1 - 0.124\left(\frac{z-400}{182}\right)^2\right],$$

such that the density ranges from 0.1 n_c to 0.25 n_c, where n_c is the critical density. Since $\lambda_\perp$ is much smaller than the density scale length in the transverse direction, the plasma is assumed to be uniform in that direction. A temperature of 0.8 keV was taken throughout the plasma.

The interaction beam is modeled by $I(t) = I_0(t)(1 + \varepsilon \cos k_\perp x)$, where $k_\perp = 2\pi/\lambda_\perp$ and $\varepsilon = 0.68$. Its temporal evolution is Gaussian with a 100-ps FWHM.

Simulation Results

Simulation results are presented here with the initial background conditions described in the previous section and three types of interaction beams, with varying spatial modulation wavelengths and peak intensities. In all cases the plasma is defined in a uniform 20×20 Eulerian grid in the x-z plane, with 18 velocity groups of size $\Delta v = 0.5(T/m)^{1/2}$ (where $T = 0.8$ keV). In view

of the symmetry of the problem, the simulation is restricted to $0 \leq x \leq \lambda_\perp/2$, with reflective boundary conditions imposed at $x = 0$ and $\lambda_\perp/2$. Zero heat flow is likewise imposed at the $z = 0$ and 400-μm boundaries, though free plasma flow is allowed there.

All simulations progress from -100 ps to 100 ps with respect to the peak of the interaction pulse. The time step and grid size were small enough to ensure converging solutions and a maximum fractional deviation from quasi-neutrality of less than 1%.

(A) $I_0 = 4.2 \times 10^{13}$ W/cm^2 and $\lambda_\perp = 42$ μm

Figure 47.16 shows a surface plot of the normalized laser intensity I/I_0 in the x-z plane at $t = -100$ ps. The plot emphasizes the initial spatial modulation of the interaction beam and shows that the beam is slightly attenuated as it propagates through the plasma.
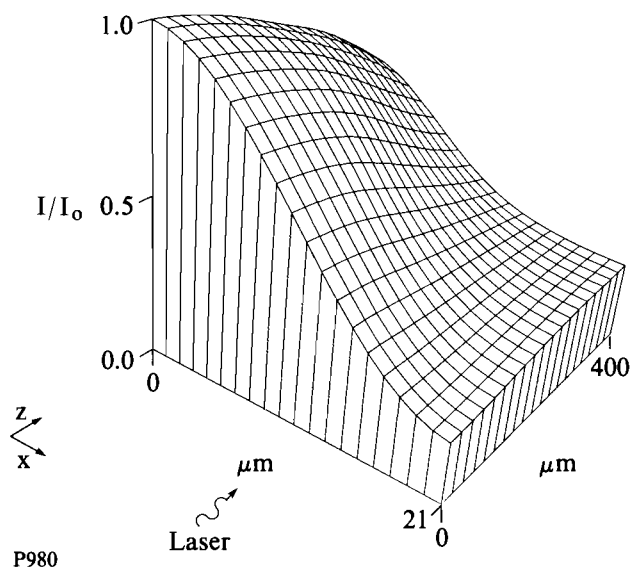

Fig. 47.16
Surface plot of normalized initial laser intensity I/I_0 on the x-z plane.

At the peak of the pulse there is significant amplification of the laser intensity due to self-focusing, as shown in Fig. 47.17(a). By comparison, the case with SH heat flow, depicted in Fig. 47.17(b), shows very little self-focusing. This gives a clear indication that nonlocal (or kinetic) heat transport plays a significant role in the filamentation process. Indeed, if one were to repeat the same simulation with the ponderomotive force artificially suppressed, the peak intensity in Fig. 47.17(a) would only go down by 30%, whereas in the classical transport case the amplification would disappear completely. The dominance of kinetic thermal filamentation can be directly attributed to the reduction in the effective heat-flow coefficient, as discussed in Ref. 5. For the present case, the ratio of the FP heat flow q_{FP} to the local q_{SH} ranges from 0.1 to 0.003 across the mesh, despite the fact that the
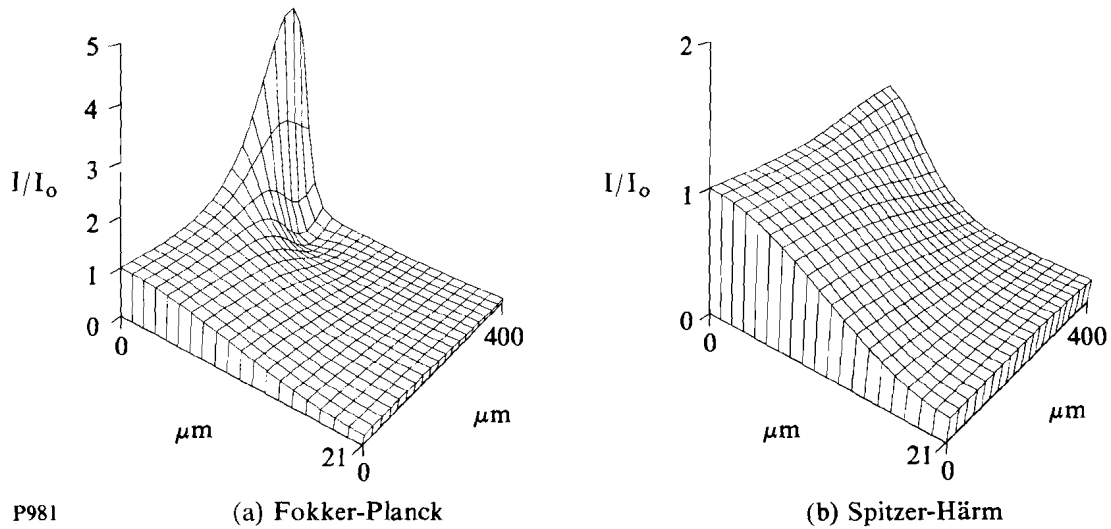
P981   (a) Fokker-Planck   (b) Spitzer-Härm

Fig. 47.17
Surface plots of I/I_0 on the x-z plane at $t = 0$ ps (i.e., at the peak of the laser pulse) for (a) Fokker-Planck transport and (b) Spitzer-Härm transport.

magnitude of q_{FP} never rises above $0.006\ q_f$, where $q_f = nm(T/m)^{3/2}$ is the so-called free-streaming limit.

The main diagnostic for filamentation in Young et al.'s experiment[4] measures density modulation, rather than intensity amplification. Therefore, $\delta n/n_0 = (n - n_0)/n_0$ [where $n_0(z)$ is the mean density averaged along x] is plotted in Figs. 47.18(a) and 47.18(b) for nonlocal and classical transport, respectively. Although $\delta n/n_0$ in Fig. 47.18(a) is somewhat smaller than the 10% measured experimentally, this discrepancy could be attributed to the uncertainties in the experimental measurement and in the quoted plasma background conditions. However, it is certainly clear that the ponderomotive force alone, which is the dominant driving mechanism in Fig. 47.18(b), yields $\delta n/n_0$ values that are more than one order of magnitude below 10%.

Another important factor in the interpretation of these simulations is the temporal evolution of the plasma. This is described in Fig. 47.19, which plots the σ_{rms} of n (i.e., the maximum rms deviation of n across x, normalized to n_0), for FP transport (solid curve) and SH transport (dashed curve) as a function of time. It is obvious from the transient nature of the curves that steady state (or pressure balance) is never achieved in the simulation. This fact could have been predicted by estimating the hydrodynamic response time of the plasma as $\tau_H = \lambda_\perp/c_s$, where c_s is the isothermal sound speed. For our conditions $\tau_H \sim 200$ ps, which is comparable to the FWHM of the laser. From the point of view of Young et al.'s experiment,[4] the probe beam was able to detect the density modulations since it was synchronized with the interaction beam (with the same 100-ps FWHM).
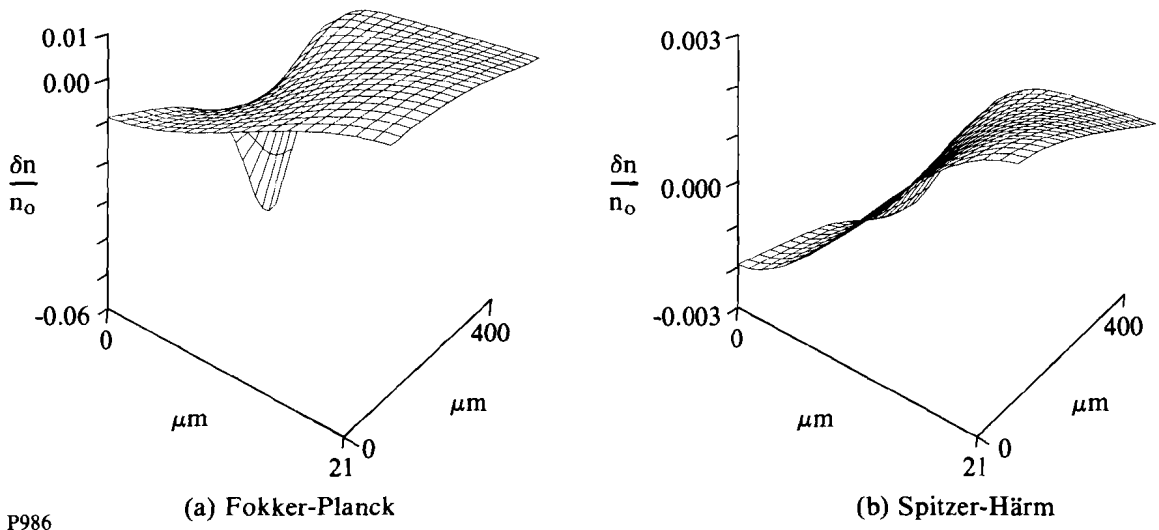
(a) Fokker-Planck

(b) Spitzer-Härm

P986

Fig. 47.18
Surface plots of normalized density modulation $\delta n/n_o$ on the x-z plane at $t = 0$ ps for (a) Fokker-Planck transport and (b) Spitzer-Härm transport. Note that $\delta n/n_o$ changes sign from < 0 at $x = 0$ (representing a depression) to > 0 at $x = 21$ μm.
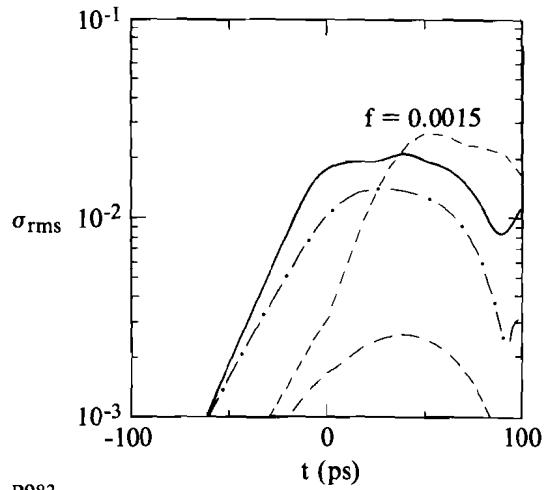
Fig. 47.19
Plot of rms density modulation σ_{rms} as a function of time, for case (A) $I_o = 4.2 \times 10^{13}$ W/cm^2 and $\lambda_\perp = 42$ μm. Solid curve corresponds to Fokker-Planck simulation, dash-dotted curve to Fokker-Planck simulation without ponderomotive force, and dashed curves to Spitzer-Härm simulation (with and without a flux limiter).

P983

To re-emphasize the dominance of the kinetic thermal-filamentation instability over the ponderomotive one, Fig. 47.19 also plots the FP simulation results without the ponderomotive force (dash-dotted curve). The corresponding curve with SH heat flow is not displayed since its $\sigma_{rms} \ll 10^{-3}$.

In an attempt to reproduce the FP results, the SH simulation was repeated by limiting the heat flux with a harmonic flux limiter, i.e., $q_{SH}/(1 + |q_{SH}/fq_f|)$.[11] It was found that $f = 0.0015$ gave the best fit, though the agreement was qualitative at best (see dashed curve identified by $f = 0.0015$ in Fig. 47.19). Another problem with the flux limiter is that the appropriate f would have to depend on $\lambda_\perp/\lambda_e$ because the amount of heat-flux inhibition due to nonlocal transport effects is dependent on $\lambda_\perp/\lambda_e$, where $\lambda_e = T^2/[4\pi n e^4(\phi Z^*)^{1/2}\ln\Lambda]$ is the effective stopping length of an electron.[12]

(B) $I_0 = 2.8 \times 10^{13}$ W/cm^2 and $\lambda_\perp = 42$ μm

These parameters for the interaction beam give rise to qualitatively similar results to case (A). As expected, the reduction in peak laser intensity has the effect of reducing the degree of self-focusing and the amount of density modulation. The temporal response of the latter is plotted in Fig. 47.20, which shows approximately a 25% reduction in the maximum σ_{rms} from that in Fig. 47.19. It is, therefore, surprising that in this case no filamentation was observed experimentally. One could speculate that this present case happens to fall just below the detection threshold of the experiment.

(C) $I_0 = 4.2 \times 10^{13}$ W/cm^2 and $\lambda_\perp = 135$ μm

In this case, no filaments were detected experimentally.[4] The results of the simulation, plotted as density σ_{rms} as a function of time in Fig. 47.21, confirm these findings. Since the hydro response time ($\tau_H \sim 600$ ps) is longer for this case than for cases (A) and (B), the density-modulation level is too low at the peak of the probe beam to be measured. The σ_{rms} eventually reaches $\sim 10^{-2}$ at $t = 100$ ps; however, by then the probe beam is too weak to detect it. Therefore, the reduction in the level of self-focusing has less to do with the spatial growth rate of the instability and more to do with the hydrodynamic response of the plasma.

Discussion and Conclusions

The results presented in this article are in qualitative agreement with the analytic kinetic theory of filamentation derived in Ref. 5, which predicted larger growth rates for the thermal rather than ponderomotive filamentation. However, quantitative comparisons have not been possible since that theory calculates linear spatial growth rates for a given transverse spatial modulation $k_\perp$, assuming momentum and energy balance. Despite the fact that $|\delta n/n_0|$ and $|\delta T/T_0| \ll 1$, the FP simulations yield $\delta I/I_0 \gg 1$ and a corresponding wide spectrum in $k_\perp$, in accordance with the narrowing of the filaments as they propagate along z. Moreover, steady-state conditions are never achieved. In fact, by observing the time behavior of the density in Fig. 47.19 one can see the onset of spatial oscillations (of period τ_H) for $t \gtrsim 100$ ps. The total amount of damping may, however, be underestimated since SPARK does not include Landau damping.[13]

Although we have only considered 2-D filamentation, in some circumstances three-dimensional effects could become important and give rise to considerably larger intensity amplifications.[14] This is specially true if "hot-
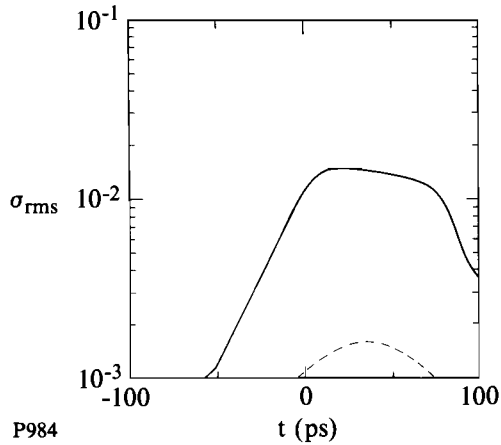
Fig. 47.20
Plot of rms density modulation σ_{rms} as a function of time, for case (B) $I_o = 2.8 \times 10^{13}$ W/cm^2 and $\lambda_\perp = 42$ μm. Solid curve corresponds to Fokker-Planck simulation, and dashed curve to Spitzer-Härm simulation.
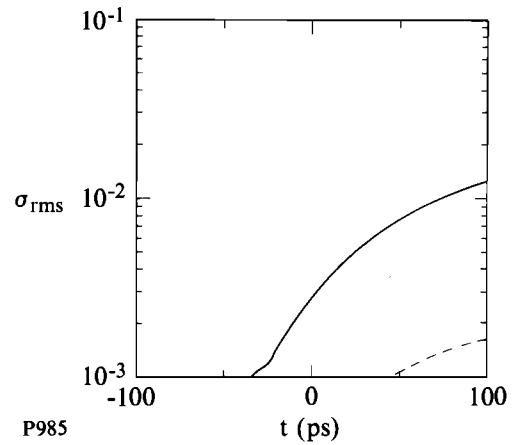
Fig. 47.21
Plot of rms density modulation σ_{rms} as a function of time, for case (C) $I_o = 4.2 \times 10^{13}$ W/cm^2 and $\lambda_\perp = 135$ μm. Solid curve corresponds to Fokker-Planck simulation, and dashed curve to Spitzer-Härm simulation.

spots" are present in the laser-intensity profile, since these may give rise to cylindrical instead of planar filaments. However, the conclusions regarding the comparison between thermal and ponderomotive filamentation are likely to remain unchanged.

The role of magnetic fields in the presence of nonuniform laser illumination has been previously studied in the context of 2-D classical heat flow and found to be negligible.[15] The effects of magnetic fields on nonlocal transport are expected to be stronger,[16] though an accurate estimation of their importance is outside the scope of this work.

In conclusion, the dominance of kinetic thermal filamentation over ponderomotive filamentation, predicted by analytic theory, has been confirmed by means of the 2-D FP code SPARK. Specific simulations using the reported conditions of Young et al.'s experiment show good agreement with their results.

REFERENCES

1. W. L. Kruer, *Comments Plasma Phys. Control. Fusion* **9**, 63 (1985); P. E. Young, *Comments Plasma Phys. Control. Fusion* **12**, 53 (1988); and references therein.

2. P. Kaw, G. Schmidt, and T. Wilcox, *Phys. Fluids* **16**, 1522 (1973).

3. M. S. Sodha, A. K. Ghatak, and V. K. Tripathi, in *Progress in Optics*, edited by E. Wolf (North Holland, Amsterdam, 1976), Vol. 13, p. 169; J. N. McMullin, C. E. Capjack, and C. R. James, *Comput. Phys. Commun.* **23**, 31 (1981).

4. P. E. Young *et al.*, *Phys. Rev. Lett.* **61**, 2336 (1988).

5. E. M. Epperlein, *Phys. Rev. Lett.* **65**, 2145 (1990).

6. B. I. Cohen *et al.*, *Phys. Fluids B* **3**, 766 (1991).

7. E. M. Epperlein, G. J. Rickard, and A. R. Bell, *Phys. Rev. Lett.* **61**, 2453 (1988); E. M. Epperlein, G. J. Rickard, and A. R. Bell, *Comput. Phys. Commun.* **52**, 7 (1988); G. J. Rickard, A. R. Bell, and E. M. Epperlein, *Phys. Rev. Lett.* **62**, 2687 (1989).

8. L. Spitzer, Jr. and R. Härm, *Phys. Rev.* **89**, 977 (1953).

9. I. P. Shkarofsky, T. W. Johnston, and M. A. Bachynsky, *The Particle Kinetics of Plasmas* (Addison-Wesley, London, 1966).

10. R. A. Gentry, R. E. Martin, and B. J. Daly, *J. Comp. Phys.* **1**, 87 (1966).

11. R. C. Malone, R. L. McCrory, and R. L. Morse, *Phys. Rev. Lett.* **34**, 721 (1975).

12. This definition of λ_e is slightly different from the one found in Ref. 5, due to the finite Z corrections currently introduced.

13. R. L. Berger, B. F. Lasinski, and E. A. Williams (private communication).

14. A. J. Schmitt, *Phys. Fluids B* **3**, 186 (1990); R. L. Berger *et al.*, in *Three-Dimensional Simulations of Filamentation* (presented at the 21st Anomalous Absorption Conference, Banff, Alberta, Canada, 15–19 April 1991).

15. A. R. Bell and E. M. Epperlein, *Plasma Phys. Control. Fusion* **28**, 897 (1986).

16. T. H. Kho and M. G. Haines, *Phys. Fluids* **29**, 2665 (1986).